energies

MDPI

Article

Pressure Fluctuations in the S-Shaped Region of a Reversible Pump-Turbine

Zijie Wang [1], Baoshan Zhu [1,*], Xuhe Wang [1] and Daqing Qin [2]

[1] Department of Thermal Engineering, State Key Laboratory of Hydro Science and Engineering, Tsinghua University, Beijing 100084, China; 13331391026@163.com (Z.W.); wangxuhe1985@163.com (X.W.)
[2] Harbin Institute of Large Electrical Machinery, Harbin 150040, China; qindq@hec-china.com
* Correspondence: bszhu@mail.tsinghua.edu.cn; Tel.: +86-10-6279-6797

Academic Editor: Hailong Li
Received: 11 June 2016; Accepted: 9 January 2017; Published: 13 January 2017

Abstract: Numerical simulations were performed to investigate pressure fluctuations in the S-shaped region of a pump-turbine model. Analyses focused on pressure fluctuations in the draft tube and in the gap between the guide vanes and runner. Calculations were made under six different operating conditions with a constant guide vane opening, and the best efficiency point, runaway point, and low-discharge point in the turbine brake zone were determined. The simulated results were compared with experimental measurements. In the draft tube, a twin vortex rope was observed. In the gap between the guide vanes and runner, a low frequency component was captured at both the runaway and low-discharge points in the turbine brake zone, which rotated at 65% of the runner frequency. This low frequency component was induced by the rotating stall phenomenon. At the runaway point, a single stall cell was found in the gap between the guide vanes and runner, while at the low-discharge point, four stall cells were observed.

Keywords: pump-turbine; pressure fluctuation; S-shaped region; vortex rope; rotating stall

1. Introduction

Pumped hydro energy storage (PHES) is currently the only proven large-scale (>100 MW) energy storage technology. There are great benefits in using PHES in electricity generation systems. Its flexibility can provide upregulation and downregulation. Its quick start capabilities make it suitable for black starts, and for providing spinning and standing reserves. Interest in this technology has recently been renewed because of the increasing use of renewable energy such as wind-powered electricity generation. Such technology is weather dependent, and so is highly variable over time [1,2].

A key component of PHES stations is the pump-turbine. Pump-turbines usually use a single runner to perform the functions of both pump and turbine. In order to adapt to the load changes of the power system, a pump-turbine is required to frequently switch between turbine mode and pump mode. This leads to extended operations in off-design operating conditions, such as at start-up and during load rejection processes. In the associated transient processes of pump-turbines, the S-shaped characteristics of the performance curves in turbine mode usually induce instability problems. The most common problems are difficulties in synchronizing with power grids during turbine start-ups, and unstable performance during turbine load rejections [3,4].

In recent years, both experimental and modelling studies have investigated the unstable flow characteristics of pump-turbines operating in off-design conditions [5–10]. Husmatuchi et al. [5,6] experimentally investigated pressure fluctuations in the gap between the guide vanes and runner. In their research, a low frequency component was observed under runaway conditions and turbine brake conditions. This low frequency instability was induced by one stall cell rotating inside the runner. Widmer et al. [7] performed numerical simulations of flows in a model pump-turbine. It was concluded

that the unstable characteristics observed with low flow masses were induced by stationary vortex formation and rotating stall. Cavazzini et al. [8] carried out a numerical analysis of the load rejection process at a constant rate, and with a large guide vane opening of a pump-turbine in turbine mode. The flow analysis showed clearly the onset and development of unsteady phenomena progressively developing into an organized rotating stall during turbine brake operations. Both experimental and numerical studies have revealed complex flow characters in the S-shaped region of pump-turbines. Such vortexes may partially block the flow [7,9,10], or cause stall cells to rotate in the runner channels at 50%–70% of the runner rotation frequency [5,6,8].

As pump-turbines operate in or near the S-shaped region, vortex ropes are inevitably formed in the draft tubes [11]. Ruprecht et al. [12] and Kirschner et al. [13] investigated unstable characteristics in the draft tube of a pump-turbine. They reported that pressure fluctuations are mainly induced by vortex ropes in the draft tube. Usually, a single-helical vortex rope is formed in the draft tube; therefore, most research has focused on regimes with a single helical vortex rope [11–13]. However, for some hydraulic turbines, at small flow masses, the single helix is replaced by a double helix, and twin vortex ropes can be formed [11,14]. One of the first detailed reports of twin vortex ropes in draft tubes was presented by Wahl [14], who was able to measure their precession frequency.

In this paper, numerical simulations are performed to study instability near, or in, the S-shaped region of a pump-turbine model operating under off-design conditions. The model runner was designed by Wang et al. [15–17] during the development of the Liyang Pumped Storage Power Station in Jiangsu Province, China. Model tests were conducted in a stand high-head test rig at the Harbin Institute of Large Electric Machinery of China. The analyses mainly focus on the pressure fluctuations and flow characteristics in the draft tube and in the gap between the guide vanes and runner. In the draft tube of the pump-turbine model, pressure fluctuations are mainly caused by a twin vortex rope. In the gap between the guide vanes and runner, a low frequency component induced by rotating stalls is captured both at runaway and low-discharge conditions.

2. Object and Research Methods

2.1. Scaled Pump-Turbine Model

The scaled model pump-turbine runner used in this study is shown in Figure 1. The model was designed in order to conduct measurements on a standard test rig. The main parameters of the model runner are listed in Table 1. The scale of the model was one-tenth of the prototype turbines installed in aforementioned Liyang Pumped Storage Power Station. The rated specific speed of both model and prototype is $n_s = 145.80$ m · Kw. The specific parameters of the prototype pump-turbine are as follows. In turbine mode, the rated head is H_r = 259 m and the rated output power is P_r = 255 MW. The rotational speed is $n_r = 300$ rpm for both turbine and pump modes. In pump mode, the maximum and minimum heads are $H_{max} = 298$ m and $H_{min} = 239$ m, respectively.

Figure 1. Model runner.

Table 1. Parameters of pump-turbine model in turbine mode.

Parameter	Value
D_2 (runner inlet diameter in turbine mode, mm)	448.2
n (runner rotating speed, rpm)	1200
Z_b (number of runner blades)	7
Z_s (number of stay vanes)	20
Z_g (number of guide vanes)	20
H_r (rated head, m)	37.68
Q_r (rated discharge, m^3/s)	0.384
n_{11} (rated unit speed, rpm)	87.62
Q_{11} (rated unit discharge, m^3/s)	0.311
n_s (rated specific speed, m·Kw)	145.80

Model tests were conducted on a standard hydraulic machinery test rig at the Harbin Institute of Large Electric Machinery, China. Figure 2 gives a schematic diagram of the model test rig. The test rig had two test stations, A and B, of which Station A could be used to conduct the model tests for Francis turbines and reversible pump-turbines. The main specifications of the test rig and the pressure sensor (PCB112A22) used for the pressure fluctuation measurement are listed in Table 2. All measurements were conducted in accordance with International Electrotechnical Commission (IEC) Standard 60193 [18].

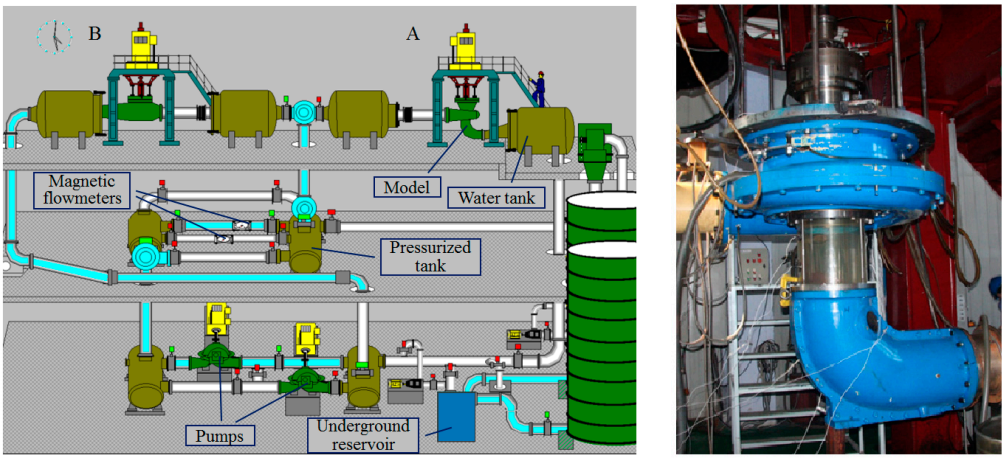

(**a**) (**b**)

Figure 2. International Electrotechnical Commission (IEC) standard test rig. (**a**) Schematic diagram; and (**b**) test section.

Table 2. Characteristics of test rig performance and pressure sensors.

Item \ Parameter	Characteristic	Value
The test rig	Maximum head (m)	150
	Maximum discharge (m^3/s)	2.0
	Runner diameter range (mm)	300–500
	Generating power (kW)	500
	Test accuracy in efficiency (%)	±0.2
Pressure sensor	Measurement range (mPa)	0.345
	Sensitivity (mv/kPa)	14.5
	Resolution (kPa)	0.007
	Sampling frequency (kHz)	0.5–250
	Constant current excitation (mA)	2–20

In Figure 3, the measured S-shaped characteristics in some smaller guide vane openings are given. Of these, the unit speed n_{11}, unit discharge Q_{11}, and unit moment M_{11} are defined as follows:

$$n_{11} = \frac{nD_2}{\sqrt{H}},\ Q_{11} = \frac{Q}{D_2^2\sqrt{H}},\ M_{11} = \frac{M}{D_2^3 H} \tag{1}$$

where n stands for the runner rotating speed, D_2 for the runner inlet diameter in turbine mode, H for the head in the model tests, Q for the discharge, and M for the moment. The four-quadrant test was conducted under a constant speed of $n = 500$ rpm. In Figure 3, only the first quadrant is illustrated, in order to clearly show the S-shaped characteristics. The normal operating range of the turbine mode is indicated by the two vertical lines.

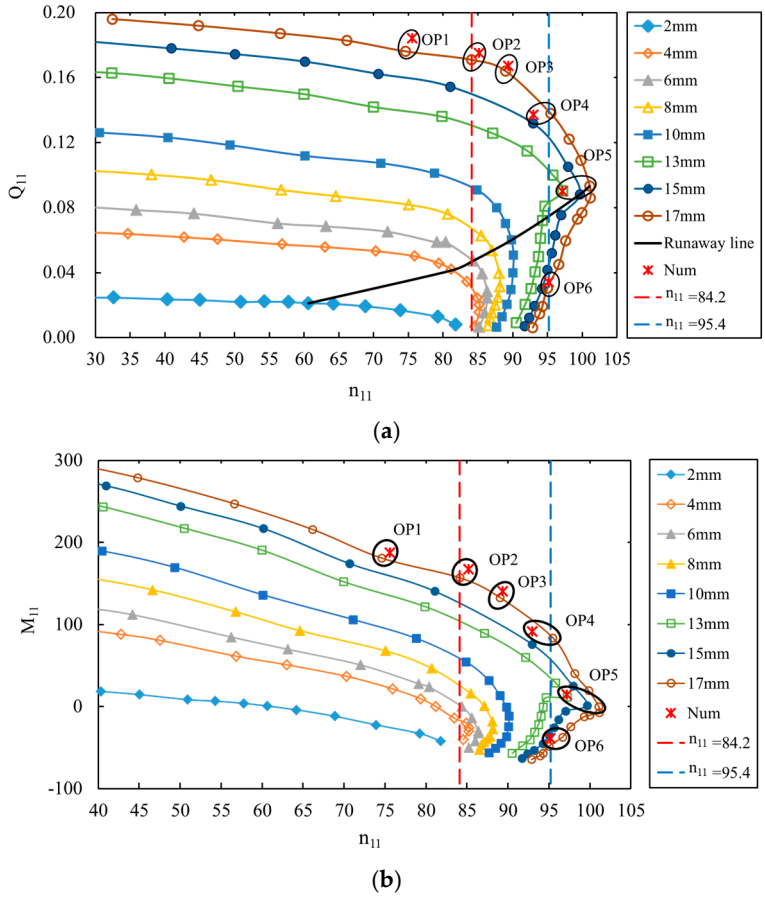

Figure 3. S-shaped curves at constant guide vane openings. (**a**) $n_{11} - Q_{11}$ characteristic curve; and (**b**) $n_{11} - M_{11}$ characteristic curve.

2.2. Numerical Solutions

Three-dimensional turbulent flow simulations were conducted for the full-passage pump-turbine. The extensively-used commercial code ANSYS CFX 15.0 (ANSYS Inc., Canonsburg, PA, USA) was used to conduct the numerical simulations.

Turbulence models are important factors in computational fluid dynamics (CFD). An advanced turbulence model, the detached eddy simulation (DES), was adopted to provide highly detailed simulations of flow patterns and unsteady phenomena. The shear stress transport $k - \omega$ model was used in the boundary layer, while the Smagorinsky-Lilly model was applied in detached regions [8].

The ANSYS ICEM (a powerful meshing software) and Turbo Grid were used for grid generation. The computational domain was divided into five parts for meshing (Figure 4), namely the spiral casing,

stay vanes, guide vanes, runner and draft tube. Structured mesh was created for all these parts except for the spiral casing tongue, where unstructured mesh was employed due to the irregular structure.

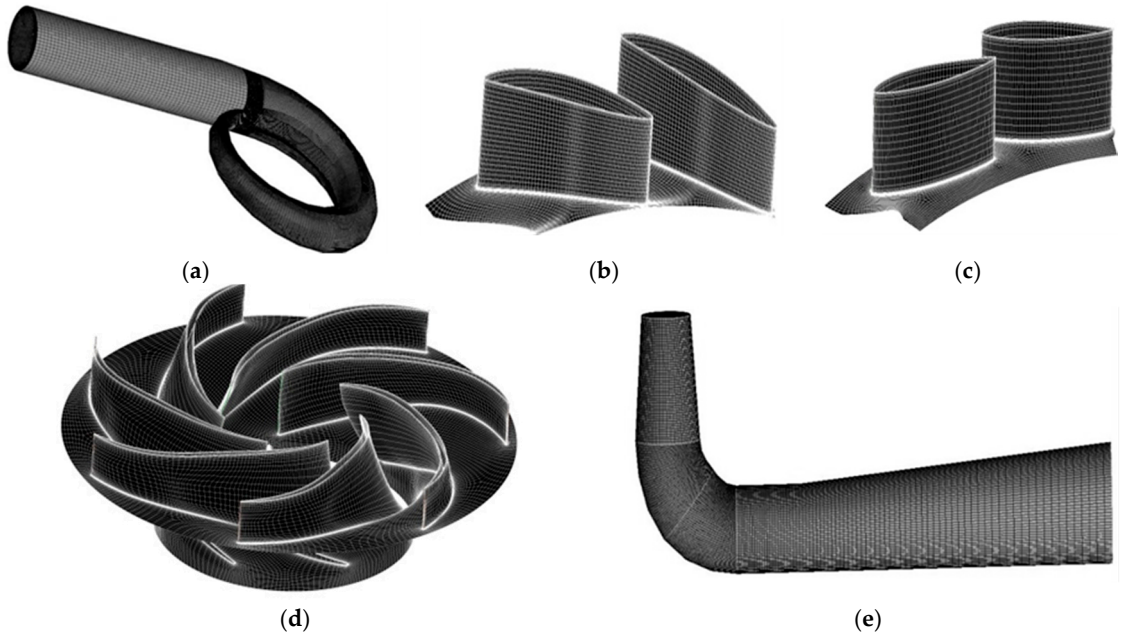

Figure 4. Boundary mesh for the full flow passage. (**a**) Spiral casing; (**b**) stay vanes; (**c**) guide vanes; (**d**) runner; and (**e**) draft tube.

At the inlet of the spiral casing, the mass flow rate was specified according to stochastic fluctuations of the velocities with a 5% free stream turbulent intensity. Static pressure was set at the outlet of the draft tube. The interfaces between stator-rotor blocks were set as the standard transient sliding interfaces. Walls were defined with no-slip wall boundary conditions. Runner blades, runner hub and shroud were fixed as rotating walls. The time-step size was set as 0.000139 s, such that one runner revolution was divided into 360 time steps. Second-order implicit time-stepping was adopted for time discretization. The convergence residuals for continuity and momentum equations were below 1.0×10^{-5}. All calculations were conducted in a cluster computer with eight Intel 5645 2.4 GHz processors, 96 GB RAM, and 2 TB hard drives (Dell Inc., Round Rock, TX, USA).

As shown in Figure 3, at a guide vane opening of $A = 17.0$ mm, OP1 is the best efficient point (BEP), OP2–OP4 are the operating points in the normal operating range, while OP5 is the runaway point and OP6 is the low-discharge point in the turbine brake. Usually, the guide vane opening is given as an angle; however, its width was used in this study. The opening angle was $\gamma = 18.0^{o}$ at A = 17.0 mm.

Four meshes (Table 3) were used to test mesh independence. The calculated points were OP2–OP4 (Figure 4). The calculated efficiency errors for OP2–OP4 are given in Table 4. Here, the error was calculated as $Err = \left(\eta_{cal} - \eta_{exp}\right)/\eta_{num} \times 100.0\%$. In the simulations, the head cover and stay ring were not included; therefore, some leakage losses and the mechanical losses were not incorporated. The calculated efficiency η_{cal} is mainly the hydraulic efficiency, and is calculated by means of a time average after the calculated unsteady condition becomes stable. Simulated results show that mesh density has a weak influence on efficiency as the grid density is high (3.62 million). After considering the complex unsteadiness, Mesh III was chosen for the simulations. The validation of the numerical results in the next section also shows that the numerical solutions used can provide reliable results.

Table 5 gives more information on Mesh III. There were a total of 4.5 million elements in the whole domain. Figure 3 shows the boundary mesh for different components. Ten element layers with normal stretching ratios were created from the walls for improving the velocity profile from the no-slip

boundaries. Near the wall, the value of no-dimensional distances was $y^+ = 50 - 180$. The mesh in the domain of the guide vanes, runner and diffuser section of the draft tube was finer than that in the other flow domain, in order to capture the complex flow characteristics in these components at higher resolution.

Table 3. Mesh densities (millions).

Component / Mesh	Spiral Casing	Stay Vanes	Guide Vanes	Runner	Draft Tube	Full Domain
Mesh I	0.50	0.45	0.35	0.41	0.47	2.18
Mesh II	0.67	0.72	0.65	0.71	0.87	3.62
Mesh III	1.00	0.45	1.20	0.98	0.87	4.50
Mesh IV	1.00	1.16	1.04	1.45	1.13	5.78

Table 4. Mesh independence checks.

Mesh / Operating Point	Mesh I	Mesh II	Mesh III	Mesh IV
OP2	5.51	2.67	2.43	1.92
OP3	7.88	4.54	3.25	3.07
OP4	10.63	5.49	4.37	3.86

Table 5. Statistics and quality of the mesh. BEP: best efficient point.

Component	Spiral Casing	Stay Vanes	Guide Vanes	Runner	Draft Tube
Mesh type	Hexahedral (except for small part near tongue in casing)				
Mesh density (millions)	1.0	0.45	1.2	0.98	0.87
Aspect ratio (0–100)	1–70.1	1–75.7	1–82.3	1–78.6	1–68.2
Mesh expansion factor (0–20)	0.1–15.4	0.1–18.1	0.1–12.3	0.1–10.6	0.1–11.8
Minimum orthogonality (0–90)	32.7	33.5	42.5	45.5	71.2
First layer thickness (mm)	1.6	1.6	0.2	0.2	1.6
Mesh incremental ratio	1.75	1.75	1.5	1.5	1.75
y^+ (at the calculated BEP)	165.0	172.5	80.3	54.1	140.8

2.3. Validation of the Numerical Results

Numerical results were compared with experimental measurements (Table 6). In the numerical simulations, the discharge Q, and the runner rotating speed n, were specified with the same values as those in the measurements, while the head H, and the moment M, were time-averaged values within the simulations. The Reynolds number was $\mathrm{Re} = \omega {D_2}^2/\nu = 2.82 \times 10^6$, where ω is the runner rotation angular velocity, D_2 is the runner inlet diameter in turbine mode, and ν is the kinematic viscosity.

The agreement between numerical and experimental results was quite good in terms of n_{11}, Q_{11}, and M_{11}, with an error less than 5.0% at OP1 and OP2–OP4. At OP5 and OP6, there was a significant increase in error (Table 5). As regards moment M, at OP5, its values should be zero, and at OP6, its value should be a small negative value. Minor numerical overestimation in the moment will induce a significant increase in errors. Moreover, mechanical friction losses were not considered in the numerical simulations. These losses are closely related to the runner rotation rate and they remain almost unchanged with the operating condition. Therefore, the corresponding reduction of hydraulic power at these two points will induce significant increases in percentage errors, as shown in Table 6. Even at these two points, the errors in n_{11} and Q_{11} are still smaller than 5.0%. This means that the hydraulic heads are still well predicted in spite of the simplification of mechanical friction losses. The comparisons demonstrate the capability of the numerical simulations to predict the hydraulic characteristics of the pump-turbine with sufficient accuracy.

Table 6. Investigated operating points and their values of n_{11}, Q_{11}, and M_{11}.

Case	Parameter	Calculation	Experiment	Error
OP1	n_{11}	75.56	74.58	1.29
	Q_{11}	0.180	0.178	1.29
	M_{11}	188.83	185.97	1.51
OP2	n_{11}	85.27	84.24	1.21
	Q_{11}	0.172	0.170	1.21
	M_{11}	157.58	152.03	3.52
OP3	n_{11}	89.56	89.26	0.33
	Q_{11}	0.163	0.162	0.33
	M_{11}	133.63	127.89	4.29
OP4	n_{11}	93.37	95.14	1.90
	Q_{11}	0.141	0.144	1.90
	M_{11}	88.93	84.99	4.43
OP5	n_{11}	97.26	101.08	3.92
	Q_{11}	0.09	0.093	3.92
	M_{11}	16.53	0.44	97.3
OP6	n_{11}	95.56	94.98	0.60
	Q_{11}	0.032	0.031	0.60
	M_{11}	-33.65	-48.26	43.4

3. Results and Discussion

Pressure monitors in the whole water passage are presented in Figure 5. Monitor SC1 was located on the spiral casing wall. In the gap between the guide vanes and runner, 20 monitors (GV1–GV20) were arranged evenly around the circumference. On the draft tube wall there were three monitors, DT1, DT2 and DT3. Pressure fluctuations on monitors GV5, GV15, and DT1–DT3 were registered in the model test [19,20]. In a pump-turbine, pressure fluctuations in turbine mode are usually stronger than those in pump mode. Moreover, fluctuation amplitudes in the draft tube and vaneless gap between the guide vanes and runner are usually larger than those in the spiral casing and stay vane channels.

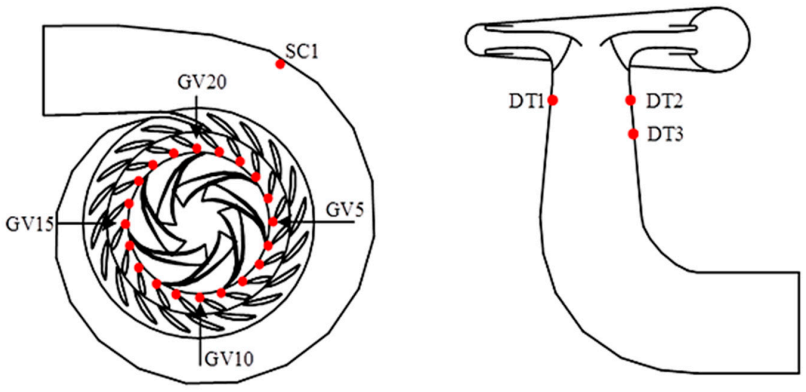

Figure 5. Pressure monitors in the whole passage.

For pressure fluctuation analyses, in frequency domains, the frequency spectrum was normalized as f/f_n, where f is the frequency component and f_n is the runner rotating frequency. In time domains, the pressure fluctuations are normalized by Equation (2).

$$\widetilde{c}_p = \frac{p - \overline{p}}{\rho E} \tag{2}$$

where $\widetilde{c}_p$ is the pressure fluctuation coefficient, p is the instantaneous pressure, $\overline{p}$ is the time-averaged pressure, and E is the specific energy.

3.1. Pressure Fluctuations in the Draft Tube

Three monitors, DT1–DT3, were located on the conical section in the draft tube. Table 7 shows the pressure fluctuations of monitor DT2 at six different operating conditions, along with the numerical and experimental results. The experimentally-measured pressure fluctuations are only listed in the table for OP2–OP4. This is because pressure fluctuations were not measured at operating points in the S-shaped region. Instead, pressure fluctuations were measured during the efficiency test [19,20]. Therefore, only the operating points in the normal operating ranges are given in the table.

Table 7. Amplitude and dominant frequency of pressure fluctuations at DT2.

Case	Amplitude (%)		Dominant Frequency (f_1/f_n)	
	Calculation	Experiment	Calculation	Experiment
OP1	5.57	-	0.82	-
OP2	8.12	6.95	0.84	0.82
OP3	9.13	7.94	0.86	0.89
OP4	8.88	10.09	1.18	1.16
OP5	3.39	-	1.19	-
OP6	0.91	-	0.75	-

Although the amplitudes have relative errors of a little more than 13.0% between numerical and experimental results, the first dominant frequency (f_1) is in good agreement. The single helical vortex rope in the draft tube usually rotates at 20%–40% of the runner rotating speed [11]. However, the dominant frequencies have higher values (Table 6). These higher frequencies may be induced by a twin vortex rope [14]. The pressure fluctuations at monitor DT2 at OP3 are shown in Figure 6a and the frequency spectrum is shown in Figure 6b. A total of 32 runner revolutions were calculated after the unsteady simulation stabilized (Figure 6). The first dominant frequency measured during the experiment was $0.89f_n$, compared with $0.86f_n$ in the simulation. Based on Table 7 and Figure 6, it can be seen that the pressure fluctuations in the draft tube are mainly induced by vortex ropes.

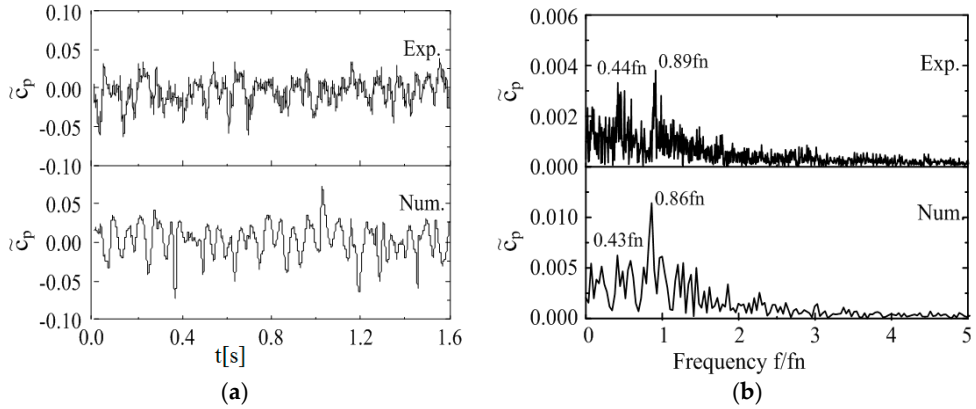

Figure 6. Measurements from monitor DT2 at OP3. (**a**) Pressure fluctuations; and (**b**) frequency spectrum.

Band-pass filtering was employed to extract the first dominant frequency component of $0.86f_n$ from the calculated pressure fluctuations of DT1, DT2 and DT3 at OP3. As shown in Figure 7, α stands for the phase difference of pressure between DT1 and DT2, and β represents the phase difference between DT2 and DT3. The α value was near zero, while β was not, which means that a twin vortex rope developed in the draft tube. If the same measurements were made at the other operating points, the twin vortex rope structure could also be detected.

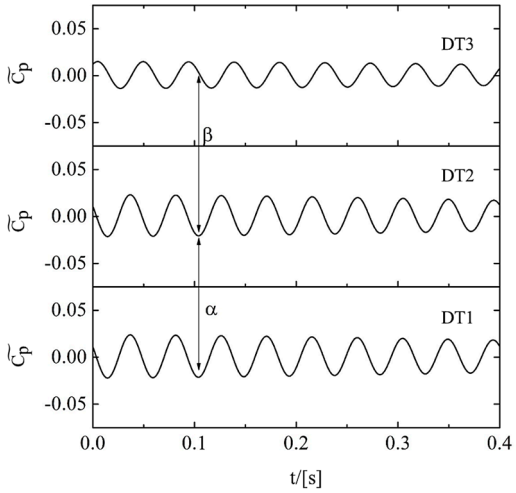

Figure 7. Band-pass-filtered pressure fluctuations at OP3.

Figure 8 shows the precession of a twin vortex rope at OP3 at a runner rotational period of T. The pressure contours at the planes where monitors DT1 and DT2 were located are also shown. The twin vortices are labelled A and B, and they rotate with the same angular velocity. This velocity corresponds to the dominant frequency of the twin vortex ropes, $0.86f_n$. Figure 9 shows a photograph of a vortex rope observed during the experiment. The twin vortex rope is generated alongside cavitation. This figure is simply used to verify the generation of twin vortex ropes because cavitation was not considered, and only a single flow field was simulated in the present study. It is well known that vortex ropes in draft tubes are usually induced by a high residual swirl in the input flow, which often forms a single helical vortex rope. Therefore, further research is required to understand the transition from a single to a double rope, and the influences of geometry on this process.

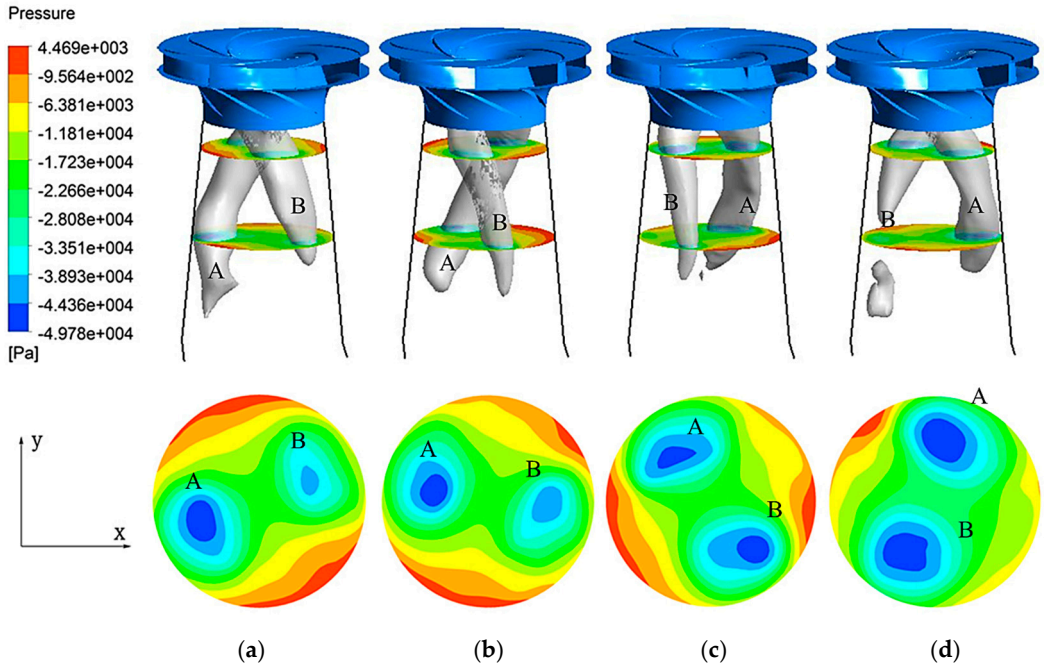

Figure 8. Twin vortex rope in the draft tube at OP3: (**a**) $t = t_0$; (**b**) $t = t_0 + 1/3T$; (**c**) $t = t_0 + 2/3T$; and (**d**) $t = t_0 + T$.

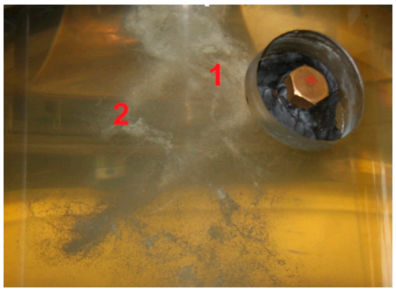

Figure 9. Photograph of a twin vortex rope taken during the experiment, with ropes 1 and 2 labelled.

3.2. Pressure Fluctuations in the Vaneless Gap

Table 8 shows the amplitude and dominant frequency of pressure fluctuations on GV5. The experimentally measured pressure fluctuations are only listed in the table for the three operation points OP2–OP4 (as per Table 7). The guide vanes and runner blades interact to generate pressure fluctuations in the gap between them. The dominant frequencies are rotor-stator interaction frequency $7f_n$ and its harmonics, for both simulated and experimental results.

Table 8. Amplitude and dominant frequency of pressure fluctuations at GV5.

Case	Amplitude (%)		Dominant Frequency (f_1/f_n)	
	Calculation	Experiment	Calculation	Experiment
OP1	5.45	-	7.00	-
OP2	5.61	6.12	7.00	7.00
OP3	8.96	10.45	7.00	7.00
OP4	35.69	30.78	7.00	7.00
OP5	35.78	-	7.00	-
OP6	28.95	-	7.00	-

The pressure amplitudes in operating conditions of low mass flow rate at OP4–OP6 were much higher than those at OP1–OP3. These increased amplitudes are believed to be induced by serious flow separation at the inlet of the runner. Figure 10 shows the distribution of streamlines at the guide vanes and runner channels under operating conditions OP1, OP5 and OP6. At OP1, the streamlines were well distributed at both guide vanes and runner channels, and there was no obvious flow separation. At OP5, flow separation occurred at the inlet of the runner, leading to backflow cells and vortices in the runner channels. However, the streamlines at the guide vanes still remained uniform. At OP6, backflow cells and vortices entirely filled the runner channels and flow separation occurred at the guide vanes.

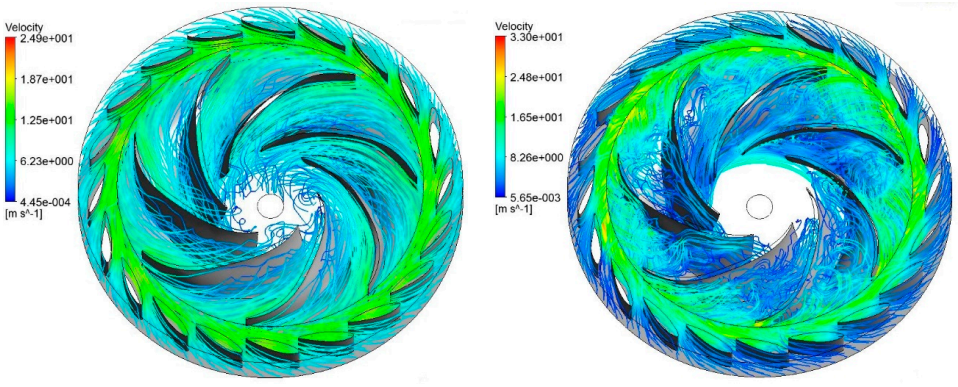

(**a**) (**b**)

Figure 10. *Cont.*

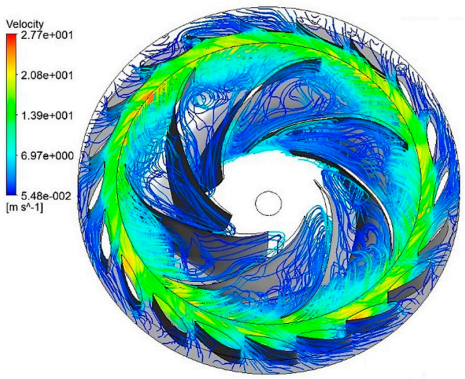

(**c**)

Figure 10. Streamlines in the guide vanes and runner. (**a**) Best efficiency point (OP1); (**b**) runaway point (OP5); and (**c**) low-discharge point (OP6).

Figure 11 presents the calculated pressure fluctuations and frequency spectrum at GV5 for operation conditions OP1, OP5 and OP6. For these three points, a low frequency component of $0.42f_n$ was captured at OP1, and $0.65f_n$ was well captured at OP5 as well as OP6, except for the blade passing frequency and its harmonics. The frequency component $0.42f_n$ at OP1 was about half of the vortex rope frequency, according to Table 6. Consequently, the component $0.42f_n$ was the rotation frequency of a single helical vortex rope. The frequency $0.65f_n$ was also well captured at the other 19 monitors in the gap between the runner and guide vanes at OP5 and OP6 (Figure 12). However, as shown in Table 7, the frequency of the twin vortex rope is different at OP5 and OP6. Therefore, the frequency $0.65f_n$ cannot be the rotation frequency of a single helical vortex rope at OP5 and OP6.

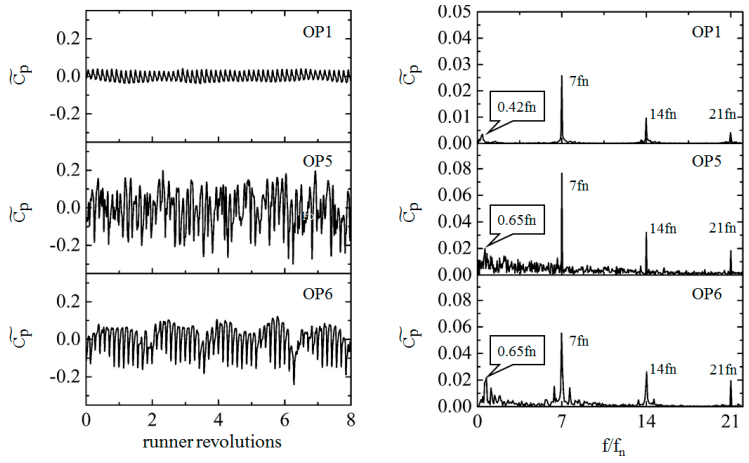

(**a**) (**b**)

Figure 11. Measurements at monitor GV5. (**a**) Pressure fluctuations; and (**b**) frequency spectra.

Figure 12 shows the band-pass-filtered pressure signals of $0.65f_n$ for monitors GV1 to GV20 at OP5 and OP6, respectively. It is mentioned by Brennen [21] that the rotating stall phenomenon may occur in one, or in a cascade of rotor or stator blades, operating at a high incidence angle. Usually, the stall appears on a few adjacent runner channels and stall cells propagate in the circumferential direction. In Figure 12, the propagation of stall cells is represented by parallel lines, and they have the same direction as the rotating direction of the runner. At OP5, there is one single stall cell in the gap between the runner and guide vanes, while at OP6, there are four stall cells. The band-pass-filtered pressure signals for the four circumferentially-distributed monitors, GV5, GV10, GV15 and GV20, are redrawn in Figure 13 for OP5 and OP6, respectively. At OP5, the pressure signals of GV5 and GV15

had a phase difference of π, which is the same as for monitors GV10 and GV20 because of a single stall cell. At OP6, as there were four stall cells all together, and there was no definite phase difference among the four monitors.

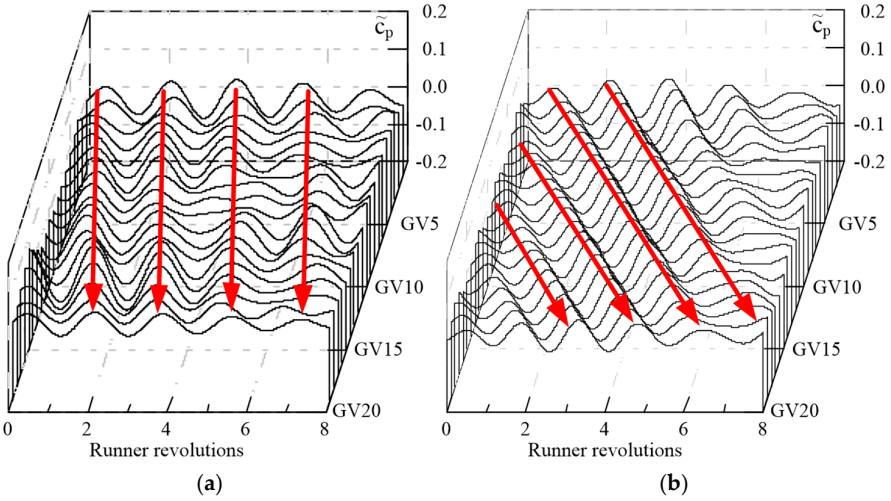

Figure 12. Propagation of rotating stall. (**a**) Runaway point OP5; and (**b**) low-discharge point OP6.

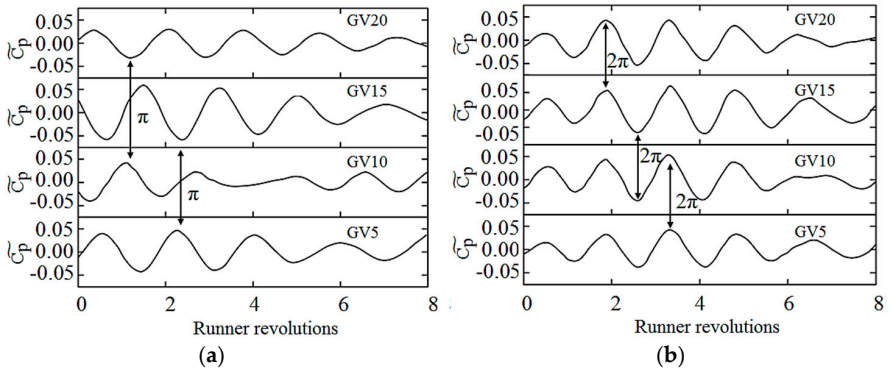

Figure 13. Band-pass-filtered pressure. (**a**) Runaway point OP5; and (**b**) low-discharge point OP6.

4. Conclusions

This study investigated flow in a reversible pump-turbine model. The unstable characteristics along a constant guide vane opening were simulated, and the numerical results were compared with experimental measurements. Analyses focused on the pressure fluctuations in the draft tube and in the gap between the runner and guide vanes. The main conclusions are summarized as:

(1) In the draft tube, a twin vortex rope formed under all the operating conditions that were investigated. The twin vortex rope rotated at 0.75–1.19 times the runner rotation speed, which was much faster than for single vortex ropes.

(2) In the gap between the runner and guide vanes, pressure fluctuations were mainly caused by rotor-stator interactions and vortices due to flow separation. A low frequency component $0.65f_n$ was well captured at both runaway and low-discharge points in the turbine brake zone, and was the effect of a rotating stall phenomenon. At the runaway point, a single stall cell was found in the gap, while at the low-discharge point, four stall cells were found.

Acknowledgments: The present work was supported by the National Natural Science Foundation of China (Grant No. 51679122). The authors would like to thank the reviewers for their constructive comments and suggestions.

Author Contributions: Zijie Wang made the computational simulations and prepared the first draft of the paper. Baoshan Zhu panned the study project, conceived, designed and performed the experiments, as well as revised the paper. Xuhe Wang contributed in the measured and calculated data analyses. Daqing Qin contributed in the experimental methodology.

Conflicts of Interest: The authors declare no conflict of interest.

References

1. Hino, T.; Lejeune, A. Pumped storage hydropower developments. *Compr. Renew. Energy* **2012**, *6*, 405–434.
2. Zhu, B.S.; Wang, X.H.; Tan, L.; Zhou, D.Y.; Zhao, Y.; Cao, S.L. Optimization design of a reversible pump-turbine runner with high efficiency and stability. *Renew. Energy* **2015**, *81*, 366–376. [CrossRef]
3. Zeng, W.; Yang, J.D.; Hu, J.H.; Yang, J.B. Guide-vane closing scheme for pump-turbine based on transient characteristics in S-shaped region. *J. Fluids Eng.* **2016**, *138*. [CrossRef]
4. Zuo, Z.G.; Fan, H.G.; Liu, S.H.; Wu, Y.L. S-shaped characteristics on the performance curves of pump-turbines in turbine mode—A review. *Renew. Sustain. Energy Rev.* **2016**, *60*, 836–851. [CrossRef]
5. Husmatuchi, V.; Farha, M. Experimental investigation of a pump-turbine at off-design operating conditions. In Proceedings of the 3rd International Meeting of the Workgroup on Cavitation and Dynamic Problems in Hydraulic Machinery and Systems, Brno, Czech Republic, 14–16 October 2009; pp. 339–347.
6. Husmatuchi, V.; Farha, M.; Roth, S.; Botero, F.; Avellan, M. Experimental evidence of rotating stall in a pump-turbine at off design conditions in generating mode. *J. Fluids Eng.* **2011**, *133*. [CrossRef]
7. Widmer, C.; Staubli, T.; Ledergerber, N. Unstable characteristics and rotating stall in turbine brake operation of pump-turbines. *J. Fluids Eng.* **2011**, *133*. [CrossRef]
8. Cavazzini, G.; Covi, A.; Pavesi, G.; Ardizzon, G. Analysis of the unstable behavior of a pump-turbine in turbine mode: Fluid-dynamical and spectral characterization of the S-shape characteristic. *J. Fluids Eng.* **2016**, *138*. [CrossRef]
9. Wang, L.Q.; Yin, J.L.; Jiao, L.; Wu, D.; Qin, D. Numerical investigation on the "S" characteristic of a reduced pump turbine model. *Sci. China Technol. Sci.* **2011**, *54*, 1259–1266. [CrossRef]
10. Sun, H.; Xiao, R.; Liu, W.; Wang, F. Analysis of the S characteristic and pressure pulsation in a pump turbine with misaligned guide vanes. *J. Fluids Eng.* **2013**, *135*, 0511011–1511016. [CrossRef] [PubMed]
11. Dörfler, P.; Sick, M.; Coutu, A. *Flow-Induced Pulsation and Vibration in Hydroelectric Machinery*; Springer: London, UK, 2014.
12. Ruprecht, A.; Helmrich, T.; Aschenbrenner, T. Simulation of vortex rope in a turbine draft tube. In Proceedings of the 21st IAHR Symposium on Hydraulic Machinery and Systems, Lausanne, Switzerland, 9–12 September 2002; pp. 259–266.
13. Kirschner, O.; Ruprecht, A.; Göde, E. Experimental investigation of pressure fluctuations caused by a vortex rope in a draft tube. *IOP Conf. Seri. Earth Environ. Sci.* **2012**, *15*. [CrossRef]
14. Wahl, T.L. Draft tube surging times two: The twin vortex phenomenon. *Hydro Rev.* **1994**, *13*, 60–69.
15. Wang, X.H.; Zhu, B.S.; Fan, H.G.; Tan, L.; Chen, Y.L.; Wang, H.M. 3D inverse design and performance investigation of a pump-turbine runner. *Trans. Chin. Soc. Agric. Mach.* **2014**, *45*, 93–98. (In Chinese)
16. Wang, X.H.; Zhu, B.S.; Cao, S.H.; Tan, L. Full 3-D viscous optimization design of a reversible pump-turbine runner. *IOP Conf. Ser. Mater. Sci. Eng.* **2013**, *52*. [CrossRef]
17. Wang, X.H.; Zhu, B.S.; Tan, L.; Zhai, J.; Cao, S.L. Development of a pump-turbine runner based on multiobjective optimization. *IOP Conf. Ser. Earth Environ. Sci.* **2014**, *22*. [CrossRef]
18. *Hydraulic Turbines, Storage Pumps and Pump-Turbines—Model Acceptance Tests*; IEC Standard 60193; International Electrotechnical Commission (IEC): Geneva, Switzerland, 1999.
19. Liu, L.; Zhu, B.; Wang, X.; Rao, C. Flow analysis of pump-turbine runner with large blade lean angle. In Proceedings of the 13th Asian International Conference on Fluid Machinery, AICFM13-127, Tokyo, Japan, 7–10 September 2015.
20. Wang, X. Multiobjective Optimization Design and Experimental Study for Reversible Pump-Turbine Runner. Ph.D. Thesis, Tsinghua University, Beijing, China, 2015. (In Chinese)
21. Brennen, C.E. *Hydrodynamics of Pumps*; Cambridge University Press: Cambridge, UK, 2011.